A Novel Method of Maximum Power Point Reaching for Magnetic Field Energy Harvesting Based on a Low-Power Analog Control Circuit

Kai Ye, Zhu Liu, Chujun Liu, Aijun Yang, *Senior Member, IEEE*, Huan Yuan, Mingzhe Rong, *Senior Member, IEEE*, and Xiaohua Wang, *Senior Member, IEEE*

***Abstract*—Magnetic field energy harvester (MEH) based on current transformers has emerged as a promising method for powering mass sensors in smart grids. However, a significant challenge lies in the insufficient power harvested at low primary currents. Aiming at resolving this shortcoming, a novel maximum power point (MPP) reaching method based on a low-power analog control circuit is proposed in the present study. The main objective of this method is to improve the performance of the MEH. The MPP is achieved by controlling the voltage of the dc side of the rectifier bridge based on the optimal load voltage characteristics of the MEH. The analog control circuit is designed using low-power analog devices and megaohm-level resistors, eliminating the need for a microcontroller. The performed analyses revealed that the calculated maximum power loss of the proposed approach is only 81.81 μW. Experimental results demonstrate a remarkable increase in MEH power output ranging from 101.39% to 149.89% compared to commercial circuits at currents ranging from 1 to 10 A.**

***Index Terms*—Low-power analog control circuit, magnetic field energy harvester (MEH), maximum power point (MPP), the optimal load voltage.**

I. Introduction

With the advancement and development of smart grids, the real-time monitoring of equipment characteristics and parameters in power systems using mass sensors has emerged as a prominent research area in recent years [1], [2], [3], [4], [5], [6], [7]. Studies show that the installation and maintenance of sensors are heavily constrained by cables and battery power. Accordingly, numerous investigations have been carried out to develop wireless sensor networks. Recently, energy harvesting technology has emerged as a highly promising technique for the development of self-powered wireless sensor networks [8], [9]. Energy harvesting techniques from the environment such as wind [10], solar radiation [11], [12], and oceanic waves [13], face limitations such as being geographically dependent or being susceptible to weather conditions. These limitations make it a challenge to provide a consistent and reliable energy supply to sensors. In contrast, power systems provide a steady and reliable source of energy including vibration [14], [15], temperature [16], and electromagnetic [17]. Among these forms of energy, vibration energy with low power density is predominantly present in power equipment with stable vibration characteristics such as transformers. Temperature energy harvesting typically exhibits poor efficiency, which limits its applicability to parts of the power systems with significant temperature variations. On the other hand, the electromagnetic field is commonly used as a reliable and continuous source of energy in power systems [18]. Another challenge associated with the electric field energy harvesting method is the requirement for a large coupling capacitor size. This is exemplified by the use of a 1 m long plate in [19]. Due to its significant energy harvesting performance, compact size, and economic feasibility, magnetic field energy harvester (MEH) technology [20], [21], [22] has emerged as an advantageous approach for powering wireless sensors.

Extensive investigations have shown that obtaining sufficient energy from the power line for sensors using the MEH technology is a significant challenge, particularly when the transmission line current is low [23]. To address this concern, comprehensive investigations have been conducted. Zhuang et al. [24] developed an augmentation technique based on control coils, injected control currents to prevent core saturation, and improved energy harvesting efficiency. Despite achieving remarkable results, the developed system was large and complicated, and the control circuit consumed a significant amount of energy. Through the use of capacitor energy storage, Liu et al. [25] significantly improved the output power of MEH. However, the control approach employed in the system, which requires detecting the primary current over zero point, is complicated to implement. Moon and Leeb [26], [27] proposed a method to increase the output power of MEH by incorporating flux-shaping capacitance and adjusting the position of the transfer window. Nevertheless, this method exhibited poor primary current adaptation, and locating

Manuscript received 6 June 2023; revised 26 September 2023; accepted 23 October 2023. Date of publication 26 October 2023; date of current version 6 December 2023. This work was supported in part by the Natural Science Basic Research Program of Shaanxi (Program No. 2023-JC-JQ-41), and in part by the Technology Program of China Southern Power Grid Company Limited under Grant Program GDKJXM20222209(036100KK52222045). Recommended for publication by Associate Editor M. Vitelli. *(Corresponding author: Aijun Yang.)*

The authors are with the State Key Laboratory of Electrical Insulation and Power Equipment, Xi'an Jiaotong University, Xi'an 710049, China (e-mail: yk1164586222@stu.xjtu.edu.cn; xajtdxlz@stu.xjtu.edu.cn; liucj1130@stu.xjtu.edu.cn; yangaijun@mail.xjtu.edu.cn; huanyuan@xjtu.edu.cn; mzrong@mail.xjtu.edu.cn; xhw@mail.xjtu.edu.cn).

Color versions of one or more figures in this article are available at https://doi.org/10.1109/TPEL.2023.3327736.

Digital Object Identifier 10.1109/TPEL.2023.3327736

the transfer window was a challenge. Furthermore, Zhuang et al. [28] enhanced the instantaneous output power of MEH for duty cycle loads. Paul et al. [29] and Wang et al. [30] conducted experiments and demonstrated that the utilization of composite core materials can enhance the output power of MEH. However, this approach has limitations as the combination of different materials in a composite magnetic core inherits both strengths and weaknesses of materials, resulting in a limited performance. A conventional method to boost the output power of MEH is to enlarge the core size. In this context, Gaikwad and Kulkarni [31] analyzed the size effect of MEH and found that increasing the core size leads to higher costs.

While most research in the field of MEH focuses on the magnetization curve to increase the output power of MEH, less research explores the concept of maximum power point (MPP) reaching in MEH to design the energy management circuit and increase the output power of MEH from different perspectives. Li et al. [32] demonstrated that impedance matching can reach the MPP for MEH. However, this approach is applicable only for resistive loads and may not meet the power supply requirements for sensor loads in energy harvesting applications. Huang et al. [33] developed an energy-tracking extraction circuit to continually reach the MPP. However, further analyses revealed that the maximum efficiency of the proposed system is up to 82%. The majority of investigations in the field of MEH use microcontrollers to reach MPPs. While this approach simplifies the design of the control system, it requires milliwatt power consumption, leading to a significant power loss. Aiming at solving the foregoing challenges, the present study focuses on analyzing the functionality of MEH to understand the relationship between harvesting power, primary current, and load voltage. To this end, a hardware circuit of MPP reaching was designed to provide a constant voltage power supply for sensors, while reducing the power consumption to the micro-watt level.

The rest of this article is organized as follows. Section II discusses the equivalent circuit of the MEH, approximate power calculation, theoretical analysis of the MPP, and experimental validation. Moreover, the fundamentals of the MPP reaching method are covered in Section III. In Section IV, the proposed technique is experimentally validated using commercial circuits. Finally, Section V concludes this article.

II. Analysis of the Optimal Load for MEH

A. Maximum Power Point Theoretical Analysis

Fig. 1 depicts the equivalent circuit for the MEH. $I_1 \sin\omega t$ is the primary sinusoidal ac current, N is the number of secondary coil turns, and $R_{\rm wire}$, $L_{\rm leak}$, and $L_{\rm m}$ are the coil resistance, leakage inductance, and excitation inductance, respectively. $V_{\rm load}$ is the constant voltage load, $I_{\rm m}$ is the excitation current, and $I_{\rm load}$ is the load current.

Since the magnetic permeability is typically high, the calculation can be simplified by ignoring the leakage inductance of the coil, the equivalent resistance of the core loss, and the excitation current of the nonsaturated core. In addition, the coil resistance has a small value and can be ignored. Consequently,

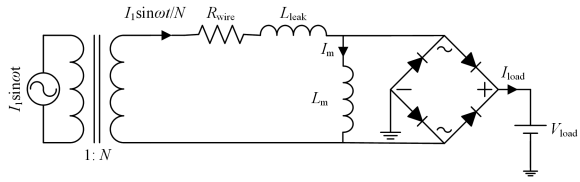

Fig. 1. Equivalent circuit of MEH.

for a primary current with a sine waveform and a frequency of $\omega/2\pi$, the amount of power delivered to the load doubles. Based on these simplifications, the output power of MEH can be expressed as follows [34]:

$$P_L = \frac{\sqrt{2} I_1 V_{\rm load} \left(1 - \cos \omega t_{\rm sat}\right)}{\pi N} \tag{1}$$

where P_L is the output power of MEH, I_1 is the primary current rms value, and $t_{\rm sat}$ is the energy transfer time of the MEH in each primary current half-cycle.

According to the electromagnetic induction principle, there is a proportional relationship between the load voltage and the rate of change of the magnetic induction in the core. At low load voltages, the MEH is capable of transmitting energy throughout the entire half cycle. However, as the load voltage increases and the magnetic induction reaches its maximum value, the MEH loses its ability to maintain the output voltage and its output capacity diminishes. According to the law of electromagnetic induction, the energy transfer can be expressed in the following form:

$$V_{\rm load} = NS\frac{dB}{dt} \tag{2}$$

where S and B are the equivalent cross-sectional area and the magnetic induction of the core, respectively. It is worth noting that the magnetic induction of the core shifts from one end of the magnetization curve to the other curve during an energy transfer cycle. Performing integration on (2) leads to the following equation:

$$\int_{-B_{\rm sat}}^{B_{\rm sat}} NS dB = \int_{0}^{t_{\rm sat}} V_{\rm load} dt. \tag{3}$$

$t_{\rm sat}$ is given by

$$t_{\rm sat} = \min\left[\frac{2NSB_{\rm sat}}{V_{\rm load}}, \frac{T}{2}\right] \tag{4}$$

where $B_{\rm sat}$ is the saturation magnetic induction and T is the primary current period. By substituting (4) into (1), the derivative can be derived as follows:

$$\frac{dP_L}{dV_{\rm load}} = \frac{2\sqrt{2} I_1}{T\omega N}\left(1 - \cos\frac{2\omega NSB_{\rm sat}}{V_{\rm load}} - \frac{2\omega NSB_{\rm sat}}{V_{\rm load}} \sin\frac{2\omega NSB_{\rm sat}}{V_{\rm load}}\right). \tag{5}$$

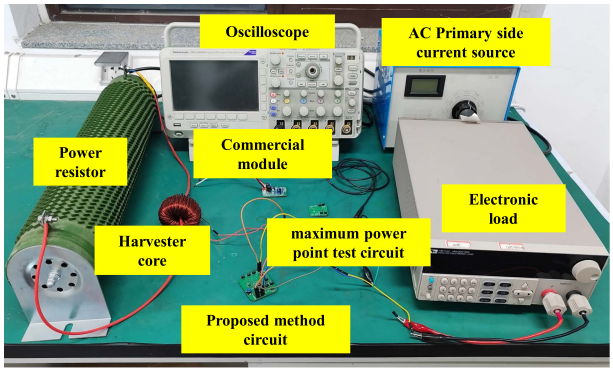

Fig. 2. Configuration of the experimental setup.

TABLE I
CORE PARAMETERS

Parameter	Value
Core material	Nanocrystalline
Core type	Toroidal
Outer radius	25 mm
Inner radius	16 mm
Height	20 mm
Saturation magnetic induction, B_{sat}	1.25 T
resistivity	115 $\mu\Omega$·cm
Equivalent cross-sectional area	140.4 mm^2
Equivalent magnetic circuit length	128.8 mm
Turns of the secondary winding	190
Frequency of the primary current	50 Hz

When (5) equals 0

$$\frac{2\omega N_2 S B_{\text{sat}}}{V_{\text{load}}} = 2.331. \tag{6}$$

Accordingly, the optimal load voltage $V_{\max}$ and the maximum output power of MEH P_{Lmax} can be obtained in the following form:

$$V_{\max} = \frac{2\omega N S B_{\text{sat}}}{2.331} \tag{7}$$

$$P_{\text{Lmax}} = 0.652 I_1 \omega S B_{\text{sat}}. \tag{8}$$

Equation (7) indicates that the optimal load voltage only depends on the characteristics of the core and the frequency of the primary current, while it is independent of its amplitude.

B. Experimental Verification of Maximum Power Point

Fig. 2 and Table I depict the configuration of the experimental setup and the core parameters. The figure includes three PCBs used for determining the MPP, testing the commercial circuit, and testing the proposed method. The isolation transformer and the power resistor are linked in series to deliver the primary current. The experimental core is crossed by the primary power line, and a rectifier bridge (in PCB called MPP test circuit) connects the two ends of the core coil to an electronic load operating at a constant voltage.

The magnetic core is modeled using Saber software, and an accurate core model is established by incorporating the nominal

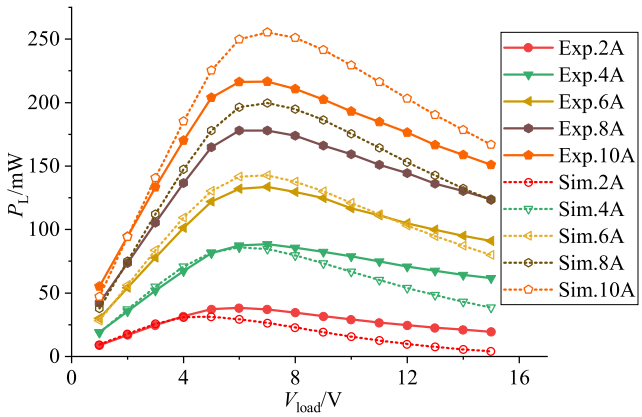

Fig. 3. Output power of MEH at different load voltages and primary currents.

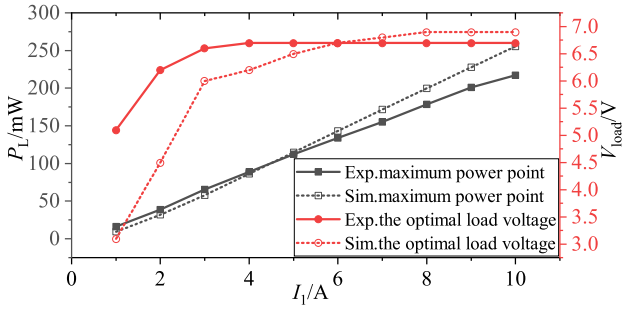

Fig. 4. Impact of primary current on the optimal load voltage and maximum power point (P_{Lmax}).

B–H curve, geometric parameters, and coil parameters of the core. However, despite these efforts, discrepancies may still occur between simulation and experimental results. These discrepancies can be attributed to various factors, including errors in the actual magnetic core parameters compared to their nominal values, measurement errors, and the challenge of accurately estimating excitation current and excitation resistance in simulation. Fig. 3 shows the output power of MEH at different load voltages and primary currents. Fig. 4 highlights the impact of primary current on the optimal load voltage and MPP. It has been observed that when the primary current exceeds 2 A, the optimal load voltage falls within the range of 6 to 8 V. Furthermore, when the load voltage fluctuates between 6 and 8 V, the output power of the MEH shows minimal variations. Consequently, when the load voltage is within this range, the MEH operates close to the MPP. On the other hand, when the primary current is 2 A and below, the optimal load voltage is reduced. However, in this case, the output power of MEH is only diminished by approximately 1–2 mW compared to the MPP at a load voltage of 6.7 V. The experimental results indicate that at 1 A and 2 A, the power at 6.7 V is 88% and 96% of the maximum power, respectively. In conclusion, it can be inferred that the optimal load voltage remains unaffected by the magnitude of the primary current, as long as it exceeds 2 A.

Although (7) indicates that the optimal load voltage is determined solely by the characteristics of the core and the frequency

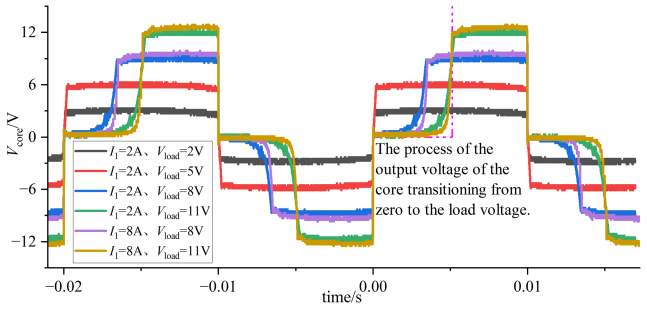

Fig. 5. Experimental results of the output voltage waveforms of the core at different load voltages and different primary currents.

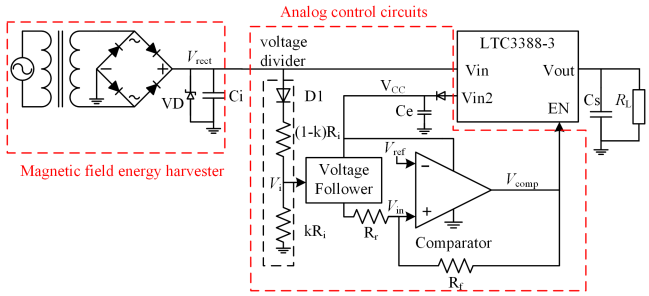

Fig. 6. Proposed system for MEH.

of the primary current, Fig. 4 reveals a correlation between the optimal load voltage and the amplitude of the primary current. The observed deviation arises because the output voltage of the core does not perfectly align with the description in (3). Equation (3) implicitly assumes that the output voltage of the core can only be zero or equal to the load voltage. However, in fact, the magnet core voltage actually undergoes a transition from zero to the load voltage, as depicted in Fig. 5. When the load voltage is low ($V_{\text{load}} = 2$ V and 5 V in Fig. 5), the core does not reach saturation throughout the entire energy transfer cycle. As a result, there is no rise in the output voltage of the core from zero to the load voltage. Instead, the output voltage of the core only changes in polarity without any change in amplitude. The output voltage waveforms of the core perfectly align with the assumption stated in (3). However, when the load voltage is high ($V_{\text{load}} = 8$ V and 11 V in Fig. 5), the core voltage drops to zero after reaching saturation. At the beginning of the next energy transfer cycle, there is a process where the core voltage rises from zero to the load voltage. This deviation from the assumption in (3) leads to a mismatch between the core voltage waveform and the equation.

The magnetization curve of the core can be approximated using the following expression [24]:

$$B = B_{\text{sat}} \times \frac{2}{\pi} \arctan \gamma H \tag{9}$$

where H is the magnetic field intensity and the γ is a constant representing the sensitivity of the core in the nonsaturation region, reflecting the initial permeability in conventional models. Because the rectifier bridge does not conduct during the process of the core voltage rising from zero to the load voltage, the excitation current is equal to the primary current. According to the Ampere circuital theorem, the magnetic field intensity can be expressed in the following form:

$$H(t) = \frac{\sqrt{2} I_1 \sin \omega t}{l} \tag{10}$$

where l is the equivalent magnetic circuit length. According to (9) and (10) and the electromagnetic induction law, the output voltage waveform of the core during the transition from zero to the load voltage can be described in the following form:

$$V_{\text{core}}(t) = \frac{2\sqrt{2}\gamma\omega I_1 N S B_{\text{sat}} \cos \omega t}{\pi l \left(1 + \frac{2\gamma^2 I_1^2 \sin^2(\omega t)}{l^2}\right)}. \tag{11}$$

During the transition of the output voltage of the core from zero to the load voltage, the rectifier bridge does not conduct, and the excitation current is equal to the primary current. Consequently, with an increase in the primary current, the excitation current also increases, leading to a shorter duration for the output voltage of the core to rise from zero to the load voltage. This phenomenon causes the output voltage waveform of the core to closely adhere to the assumption stated in (3), as illustrated in Fig. 5 ($I_1 = 2$ A and 8 A). In summary, the optimal load voltage converges toward a constant value determined solely by the characteristics of the core and the frequency of the primary current, as demonstrated in Fig. 4. Furthermore, due to the high magnetic permeability of the core, typically a small primary current is sufficient to maintain the optimal load voltage at an approximately constant value. For instance, in this case, as long as the primary current exceeds 2 A, the optimal load voltage can be considered as a constant value.

III. Proposed MEH System and Implementation

A. Proposed MEH System

Fig. 6 depicts the design of an MEH system with analog control circuits. A full-bridge rectifier is used to change the ac output into a dc output. It should be indicated that the dc–dc converter and analog control circuit are parts of the power management circuit. The analog circuit consists of a voltage divider, a voltage follower, and a comparator for MPP reaching. The circuit implementation described in this study utilizes analog components, eliminating the need for a programmable controller and significantly reducing power loss.

In the analog control circuit, the load voltage (V_{rect}) is sampled through resistor-based voltage division to obtain V_{i}. Next, V_{i} is passed through a voltage follower and compared with a predetermined reference voltage, V_{ref}, using a hysteresis comparator. Based on the comparison result, the EN terminal of the dc–dc converter is controlled to regulate the charging and discharging of capacitor C_{i}. This mechanism guarantees that the load voltage consistently remains close to the optimal load voltage. By simulating the functionality of the dc–dc converter using resistors and MOSFETs, and controlling the ON/OFF switching of the MOSFETS to simulate the controlled state of the EN terminal of the dc–dc converter, the simulation results for V_{rect} depicted in Fig. 7 were obtained. The simulation results demonstrate that the load voltage undergoes periodic fluctuations around the optimal

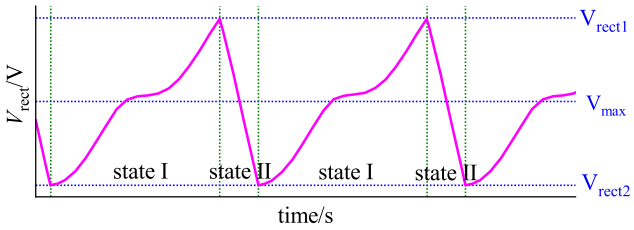

Fig. 7. Simulation result of $V_{\rm rect}$.

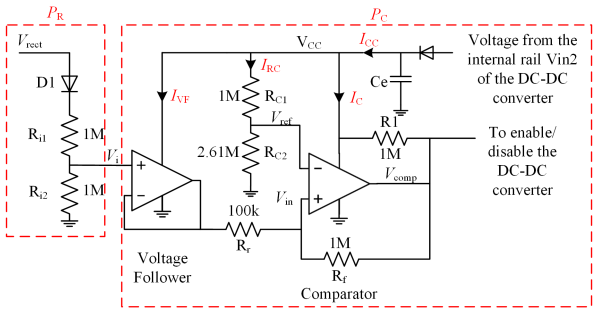

Fig. 8. Block diagram of the analog control circuit.

load voltage, oscillating between an ascending phase (State I) and a descending phase (State II). In State I, the dc–dc converter is in a disabled state, the output of the comparator is low, and the input terminals of the comparator do not draw any current. Therefore, according to Kirchhoff's law, $V_{\rm in}$ is

$$V_{\rm in} = \frac{R_f}{R_r + R_f} V_i. \tag{12}$$

Similarly, since the voltage follower does not draw any current, according to Kirchhoff's law

$$V_i = k(V_{\rm rect} - V_{D1}). \tag{13}$$

Therefore, $V_{\rm in}$ can be expressed in the following form:

$$V_{\rm in} = \frac{R_f}{R_r + R_f} k(V_{\rm rect} - V_{D1}). \tag{14}$$

As $\rm R_i$ is a megohm resistor and the EN pin of the dc–dc converter is not enabled, it can be considered that capacitor $\rm C_i$ is disconnected from the circuit behind it. In this case, $\rm C_i$ is charged by the MEH through the rectifier, resulting in an increase in $V_{\rm rect}$, $V_{\rm i}$, and $V_{\rm in}$. When $V_{\rm in}$ exceeds $V_{\rm ref}$, $V_{\rm comp}$ outputs a high level, enabling the EN pin of the dc–dc converter and causing the circuit to enter State II. During the state transition of the circuit, when $V_{\rm in}$ and $V_{\rm ref}$ are equal, the state transition threshold voltage $\rm V_{rect1}$ can be obtained according to (14).

$$V_{\rm rect1} = \frac{R_r + R_f}{kR_f} V_{\rm ref} + V_{D1} \tag{15}$$

In State II, the EN terminal of the dc–dc converter is enabled, allowing energy to be transferred from capacitor $\rm C_i$ to the load through the converter. Consequently, both $V_{\rm rect}$ and $V_{\rm i}$ decrease, leading to a decrease in $V_{\rm in}$ as well. It should be noted that, due to the high output level of $V_{\rm comp}$, according to Kirchhoff's law, the value of $V_{\rm in}$ will be determined by both $V_{\rm i}$ and $V_{\rm comp}$ as

$$V_{\rm in} = \frac{R_f}{R_r + R_f} V_i + \frac{R_r}{R_r + R_f} V_{\rm comp}. \tag{16}$$

Combined with (13)

$$V_{\rm in} = \frac{R_f}{R_r + R_f} k(V_{\rm rect} - V_{D1}) + \frac{R_r}{R_r + R_f} V_{\rm comp}. \tag{17}$$

When $V_{\rm in}$ drops below $V_{\rm ref}$, the output of the comparator becomes low, disabling the dc–dc converter and transitioning the circuit back to State I. During the circuit state transition, $V_{\rm in}$ and $V_{\rm ref}$ are equal, which gives us the state transition threshold voltage $V_{\rm rect2}$ as follows:

$$V_{\rm rect2} = \frac{R_r + R_f}{kR_f} \left(V_{\rm ref} - \frac{R_r}{R_r + R_f} V_{\rm comp} \right) + V_{D1}. \tag{18}$$

After the circuit transitions into State I, $V_{\rm rect}$ rises again. Then, $V_{\rm rect}$ moves periodically between $V_{\rm rect1}$ and $V_{\rm rect2}$. The MEH always operates at the MPP when $V_{\rm rect1}$ and $V_{\rm rect2}$ are near the optimal load voltage.

B. Power Supply for Analog Control Circuits

Fig. 8 illustrates the composition of the analog control circuit, which includes the power source provided by the internal rail $V_{\rm in2}$ of the dc–dc, capacitor $\rm C_e$, voltage follower, comparator, diodes, and resistors. The internal power supply $V_{\rm in2}$ of LTC3388-3 eliminates the need to add an additional component, such as a linear regulator, to provide power for the analog control circuit, reducing the complexity and power loss in circuit design. It can supply power regardless of whether the dc–dc converter is enabled. Moreover, the LTC3388-3 achieves high efficiency at low load current (95% at $I_{\rm load} = 100\,\mu$A) and consumes only 720 nA typical dc supply current at no load. This is particularly important for energy harvesting applications. When the converter is disabled, $V_{\rm in2}$ can provide a regulated voltage of 4.6 V from the input voltage $V_{\rm rect}$. This enables the proposed system to self-start using input power directly from the MEH, unless the output power of MEH is extremely low, below the energy consumption of the megohm voltage divider branch circuit. $V_{\rm in2}$ remains equal to $V_{\rm rect}$ up until it reaches 4.6 V, and $V_{\rm rect}$ exceeds 4.6 V, $V_{\rm in2}$ stabilizes at 4.6 V. Meanwhile, when $V_{\rm rect}$ is lower than 4.6 V, $V_{\rm in2}$ fluctuates. To ensure stable supply voltage to the analog control circuit, a diode (BAT60A) and capacitor $\rm C_e$ are included in the circuit. Capacitor $\rm C_e$ maintains the supply voltage at around 4.3 V, accounting for the forward diode voltage drop. On the other hand, the diode prevents reverse current flow from the capacitor to the dc–dc converter when $V_{\rm rect}$ falls below 4.3 V. Consequently, even if the voltage supplied by the internal rails of the dc–dc converter suddenly drops, $\rm V_{cc}$ remains stable at a reasonable level. The model of capacitor $\rm C_e$ is 25TQC22MV, and its equivalent series resistance is only 45 mΩ, which makes its power loss very low. The capacitance value is 22 μF, and it can be selected according to the recommendations in the LTC3388-3 device manual.

C. Voltage Divider Branch Circuit

The voltage divider branch comprises a starting diode (BAT60A) and two resistors. Diode D1 ensures the self-starting of the analog control circuit and the dc–dc converter. During the initial activation or restart of MEH, the voltage of the capacitor C_i is close to zero, leading to a negligible power output from the MEH to C_i. In this scenario, if the voltage divider branch resistance is high, the system may face difficulties in starting. This is because the output power generated by the MEH is fully consumed so the voltage across the capacitor C_i cannot increase. To resolve this problem, the diode D1 breaks the voltage divider branch when the voltage on C_i is lower than 0.3 V, allowing a gradual climb to 0.3 V. The voltage can continue to increase due to the high-megohm resistance of the voltage divider branch, which limits power consumption. Therefore, the system can start smoothly. Based on these descriptions, increasing the megohm level of the resistor reduces power consumption in the circuit, while it does not affect the voltage divider function.

D. Voltage Follower

To mitigate the influence of other resistors on the voltage divider circuit, its output voltage is coupled to a voltage follower. The voltage follower model is MCP6042T-I, which features low quiescent current (600 nA) and the ability to operate in a wide supply voltage range (1.4–6.0 V). This allows for extremely low power consumption and easy startup, reducing its requirements on the power supply. Its output is wired through a resistor to the comparator's in-phase end.

E. Comparator

The out-phase end of the comparator is connected to V_{ref}. The voltage V_{cc} is divided by two resistors (R_{C1} and R_{C2}) to produce the voltage V_{ref}. The in-phase terminal of the comparator is linked to the outputs of the voltage follower and the comparator through the corresponding resistors R_r and R_f. The circuit has distinct state transition threshold voltages (V_{rect1} and V_{rect2}) in different states (State I and State II) due to the feedback of the comparator output voltage. The ratio of the resistors R_r and R_f affects the difference between the two state transition threshold voltages in the circuit. If this difference is too large, the voltage swings too much around the optimal load voltage so the MPP reaching becomes less effective. Finally, the enable side of the dc–dc converter receives the comparator's output. The comparator's model is TLV3401IDBVR, which requires only 470 nA of supply current per channel. It has a wide operating supply voltage range from 2.5 to 16 V, and for harsh environments, the input voltage can be taken 5 V above the positive supply voltage without damaging the device. The low supply current makes it an ideal choice for comparators where quiescent current is the primary concern.

F. Parameter Determination Method

When determining the parameters for the circuit, two principles should be followed. The first principle is to set the state transition threshold voltages (V_{rect1} and V_{rect2}) close to the optimal load voltage. The second principle is that the difference between two state transition threshold voltages should not be too large. The average value V_{ave} and the difference ΔV_{rect} between the two transition threshold voltages can be calculated using (15) and (18).

$$V_{\text{ave}} = \frac{R_r + R_f}{kR_f}\left(V_{\text{ref}} - \frac{R_r}{2(R_r + R_f)}V_{\text{comp}}\right) + V_{D1} \quad (19)$$

$$\Delta V_{\text{rect}} = V_{\text{rect1}} - V_{\text{rect2}} = \frac{R_r}{kR_f}V_{\text{comp}}. \quad (20)$$

In the present study, the following approach is utilized to satisfy the two principles. First, V_{ave} equals the optimal load voltage, and second, ΔV_{rect} is less than half the length of the load voltage interval (V_{int}). This approach allows the MEH to operate close to the MPP.

$$\frac{R_r + R_f}{kR_f}\left(V_{\text{ref}} - \frac{R_r}{2(R_r + R_f)}V_{\text{comp}}\right) + V_{D1} = V_{\max} \quad (21)$$

$$\frac{R_r}{kR_f}V_{\text{comp}} \le \frac{1}{2}V_{\text{int}}. \quad (22)$$

The proposed method involves only one inequality constraint and one equation, making the parameter selection process relatively simple. With four unknown parameters (R_r, R_f, k, and V_{ref}), the goal is to choose a set of parameters that satisfy the requirements.

TABLE II
PLATFORM PARAMETERS

Parameter	Value
Core secondary coil resistance	2.5 Ω
Zener	LMSZ5238BT1G
Diode	BAT60A
DC–DC converter	LTC3388
Isolated Voltage Regulated Power Supply	STG-2000W
Full-bridge diode rectifier	BAS4002ARPP
Electronic load	IT8511A+
Operational amplifier	MCP6042T-I/SN
Comparer	TLV3401IDBVR

IV. EXPERIMENTATION AND EVALUATION

A. Maximum Power Point Reaching Experiment

Fig. 2 depicts the experimental platform for MPP reaching MEH. Tables I and II indicate the parameters linked to the experimental core and platform, respectively. During the experiments, the optimal load voltage was 6.7 V, and V_{int} and ΔV_{rect} were set to 2 V and 0.86 V, respectively. The analog control circuit resistance parameters are presented in Fig. 8.

Fig. 9 shows the voltage waveforms at significant points while the analog control circuit is operating. It can be observed that the load voltage (V_{rect}) undergoes periodic changes between V_{rect1} and V_{rect2}, divided into an ascending phase (State I) and a descending phase (State II). In State I, the comparator (V_{comp}) outputs a low level, the EN terminal of the dc–dc converter is not enabled, and energy is transferred from the magnetic energy harvester to the capacitor C_i. As a result, the load voltage

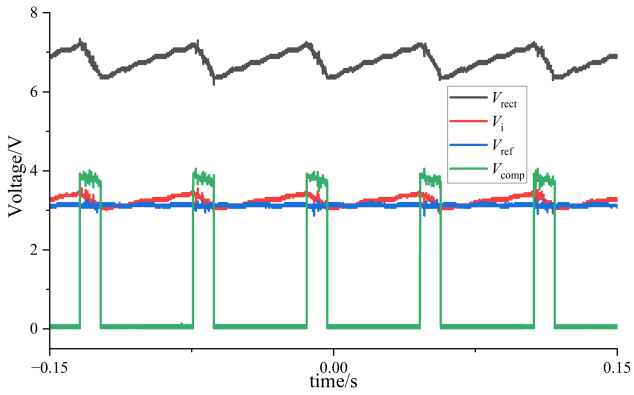

Fig. 9. Waveforms of $V_{\rm rect}$, $V_{\rm i}$, $V_{\rm ref}$, and $V_{\rm comp}$ ($I_1 = 2\,{\rm A}$, $R_{\rm L} = 100$).

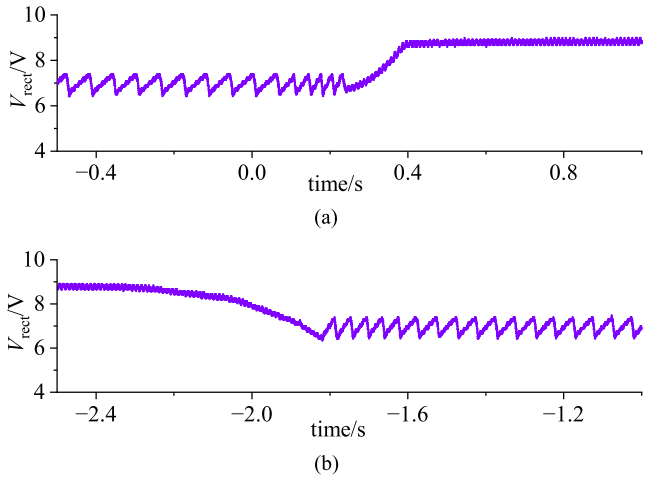

Fig. 10. $V_{\rm rect}$ waveforms when the primary current changes. (a) Increase of low current (2 A) to high current (10 A). (b) Decrease of high current (10 A) to low current (2 A).

increases, and $V_{\rm i}$, as a sample of the load voltage, also increases. According to (12), when $V_{\rm i}$ exceeds 10/9 $V_{\rm ref}$, or when $V_{\rm in}$ exceeds $V_{\rm ref}$, $V_{\rm comp}$ outputs a high level, and the circuit enters State II. In State II, $V_{\rm comp}$ outputs a high level, the EN terminal of the dc–dc converter is enabled, and energy is transferred from the capacitor $C_{\rm i}$ to the load. Consequently, the load voltage decreases, and $V_{\rm i}$ decreases accordingly. According to (16), $V_{\rm in}$ also decreases. When $V_{\rm in}$ falls below $V_{\rm ref}$, $V_{\rm comp}$ outputs a low level, the EN terminal of the dc–dc converter is not enabled, and the circuit returns to State I, repeating the cycle. During the process, the average value of $V_{\rm rect}$ was 6.88 V, which is close to the optimal load voltage. Meanwhile, the maximum and minimum values were 7.32 V and 6.44 V, respectively, resulting in a difference of 0.88 V between the extreme values.

The analog control circuit exhibits excellent stability and adaptability under different primary currents. When the primary current is low, $V_{\rm rect}$ varies between $V_{\rm rect1}$ and $V_{\rm rect2}$, ensuring that MEH operates near the MPP. Fig. 10(a) shows that as the primary current increases, $V_{\rm rect}$ rises to limit the power delivered by the MEH according to the requirements of the load or to dissipate excess power through the Zener diode. Fig. 10(b) shows

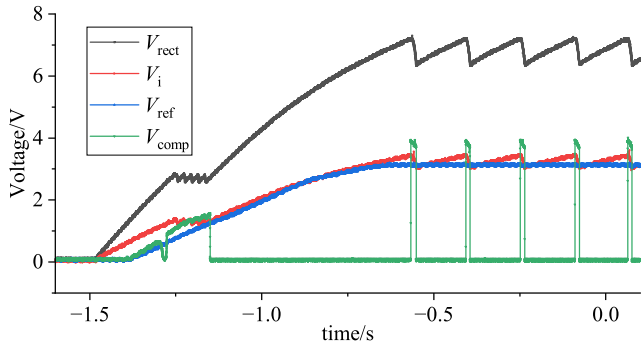

Fig. 11. Transient start-up of the analog control circuit ($I_1 = 2\,{\rm A}$, $R_{\rm L} = 100$).

that when the primary current decreases from a high value to a low value, the MEH enters State I after dropping to $V_{\rm rect2}$ and returns to a small current operation.

B. Start-Up of Analog Control Circuits

Fig. 11 depicts the transient voltage of the circuit over time. It is observed that the initial voltage of each capacitor is zero. As the MEH generates power, $V_{\rm rect}$ and $V_{\rm i}$ gradually increase from zero, whereas the dc–dc converter remains inactive and the analog control circuit consumes minimal power. $V_{\rm rect}$ charges the capacitor $C_{\rm e}$, thereby increasing $V_{\rm CC}$ and $V_{\rm ref}$. This process occurs through the internal pin $V_{\rm in2}$ of the dc–dc converter and the diode. Once $V_{\rm CC}$ reaches the startup voltage of the comparator, the output voltage $V_{\rm comp}$ is initialized to zero. However, it quickly becomes high when $9/10V_{\rm i}$ exceeds $V_{\rm ref}$. Once $V_{\rm rect}$ reaches the startup voltage of the dc–dc converter, the converter is activated and both $V_{\rm rect}$ and $V_{\rm i}$ stop rising, while $V_{\rm ref}$ rises continuously until it reaches $V_{\rm i}$. Afterward, the output voltage of the comparator becomes low, which turns OFF the dc–dc converter and leads to a steady-state operation of MEH.

C. Calculation of the Maximum Power of Analog Control Circuits

Fig. 8 shows that the power used by the analog control circuit can be primarily divided into two parts: the power P_R used by the diode D1 and resistors R_{i1} and R_{i2}, and the power $P_{\rm CC}$ used by $V_{\rm CC}$. Since $V_{\rm rect}$ can only reach a maximum of 7.32 V and $V_{\rm D1}$ is 0.3 V, and the corresponding power $P_{\rm R}$ is lower than 26 μW. This consumption is significantly lower than the output power of MEH Given by

$$P_R = \frac{V_{\rm rect}\left(V_{\rm rect} - V_{D1}\right)}{R_{i1} + R_{i2}}. \tag{23}$$

The maximum value of the power $P_{\rm CC}$ can be estimated based on the maximum value of $I_{\rm CC}$ as follows:

$$P_{CC}\left(t\right) = V_{CC}\left(t\right) I_{CC}\left(t\right). \tag{24}$$

The current $I_{\rm CC}$ comprises the currents $I_{\rm VF}$ flowing through the voltage follower, $I_{\rm RC}$ through the resistor, and $I_{\rm C}$ through the comparator branch. The currents in each component can be

TABLE III
COMPARISON OF INDICATORS BETWEEN THE PROPOSED METHOD AND EXISTING METHODS

Refs.	Control circuit	Power supply of control circuit	Load of MEH	Power loss of control circuit
[24]	LAUNCHXL-F28377S microcontroller to control the high-power control coil	Self-powered	Without dc–dc	34 mW
[25]	Controlled switches with a microprocessor of MSP430	Externally powered	Without dc–dc	unknown
[26]	PIC18F14K50 microcontroller to control the FET	Externally powered	Without dc–dc	2.63 mW
[32]	A microcontroller STM32C8T6 is used to generate the corresponding PWM wave	Externally powered	Without dc–dc	63.4751 mW
This work	Low-power analog control circuit without microcontroller	Self-powered	With dc–dc	81.81 μW

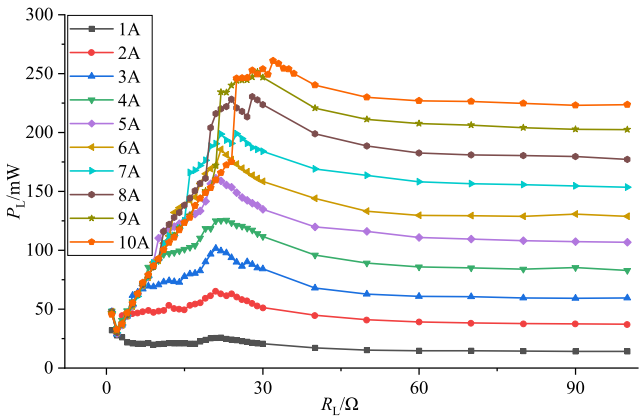

Fig. 12. Distribution of the output power of MEH against load resistance at different primary currents.

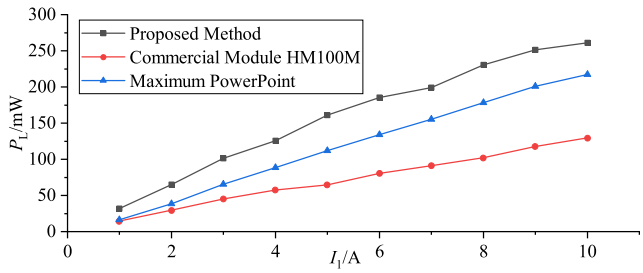

Fig. 13. Experimental results.

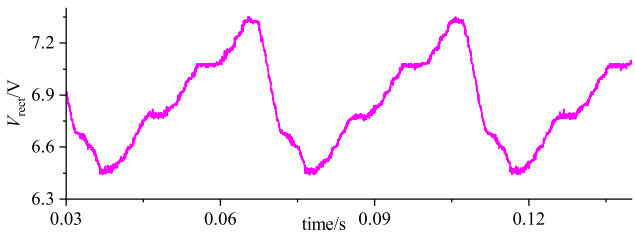

Fig. 14. $V_{\rm rect}$ waveform ($I_1 = 2$ A, $P_{\rm L} = P_{\rm Lmax}$).

expressed as follows:

$$I_{\rm VF} = I_{\rm QVF} + \frac{|V_i - V_{\rm comp}|}{R_r + R_f} \leq 3.79\ \mu{\rm A} \tag{25}$$

$$I_{RC} = \frac{V_{CC}}{R_{C1} + R_{C2}} = 1.19\ \mu{\rm A} \tag{26}$$

$$I_C \leq I_{QC} + I_{\rm EN} + \frac{V_{CC} - V_{\rm comp}}{R_1} + \frac{|V_i - V_{\rm comp}|}{R_r + R_f} \leq 8.00\ \mu{\rm A} \tag{27}$$

where $I_{\rm EN}$ is the drive current of the enabling side of the dc–dc converter, and $I_{\rm QVF}$ and $I_{\rm QC}$ are the quiescent currents of the voltage follower and comparator, respectively. Based on these equations, the maximum current $I_{\rm CC}$ is 12.98 μA, and the maximum $P_{\rm CC}$ value is 55.81 μW. Meanwhile, the estimated maximum power consumption of the analog control circuit is 81.81 μW.

D. Method Performance Evaluation

Fig. 12 displays the experimental results of the MPP reaching method. It depicts the impact of load resistance on energy harvesting from the MEH. It is observed that when the load resistance is too low, the output voltage of the dc–dc converter decreases significantly, which reduces the energy conversion efficiency and decreases the power obtained by the load.

Fig. 13 compares the MPP of MEH obtained from the proposed method with that of a commercial energy management circuit (HM100M Hemi Electronics, China). The commercial circuit operates away from the MPP, resulting in lower output power. In contrast, the proposed method achieves higher power output by operating closer to the MPP. Moreover, the use of a lower convex function in the voltage waveform of the core, as illustrated in Fig. 14, is beneficial in decreasing core saturation and increasing the ability to harvest magnetic field energy [26]. This contributes to the higher output power of MEH compared to the MPP.

E. Comparison With Existing Methods

In other energy harvesting technologies, the MPP is typically influenced by variable parameters [35], [36]. For example, in piezoelectric energy harvesting, the MPP is affected by frequency variations [37], [38], [39]. However, in MEH technology, the system frequency remains constant, and the MPP is solely determined by the properties of the magnetic core. Table III compares the proposed method with existing MEH methods in terms of the control circuit and load. Compared to other

techniques used to reach the MPP in MEH, the proposed method stands out by achieving self-powering with power consumption as low as microwatts (compared to milliwatts in other methods), and it does so without the need for a microcontroller. Furthermore, when compared to other approaches for improving the output power of MEH, the utilization of a dc–dc converter instead of directly connecting a resistor after the rectifier bridge provides a more practical and feasible solution. For instance, the effectiveness of the method presented in [26] depends on the stable load voltage provided by a constant voltage source, and the introduction of a dc–dc converter would impact the method's performance.

V. Conclusion

This study proposes a method to achieve the MPP for MEH technology, aiming to reach the MPP of MEH under different primary currents and loads. Through theoretical analysis of the output power of the MEH, it is determined that, under certain approximate conditions, the optimal load voltage is only related to the properties of the magnetic core and the frequency of the primary current. Through simulations and experiments, it is verified that due to the high magnetic permeability of the magnetic core, as long as the primary current is not very small, the optimal load voltage hardly changes with the variation of the primary current. Under the experimental conditions of this article, the optimal load voltage can be considered a constant value as long as the primary current exceeds 2 A. The proposed method achieves the MPP for MEH by designing an analog control circuit that ensures the load voltage fluctuates around the optimal load voltage. Experimental results show that compared to commercial circuits, the proposed method can increase the output power of MEH by 101.39%–149.89% in the current range of 1–10 A. Furthermore, the power consumption of the analog control circuit is estimated to be only 81.81 microwatts, which has a negligible impact on the milliwatt-level output power of MEH.

References

[1] A. E. Espe, T. S. Haugan, and G. Mathisen, "Magnetic field energy harvesting in railway," *IEEE Trans. Power Electron.*, vol. 37, no. 7, pp. 8659–8668, Jul. 2022, doi: 10.1109/TPEL.2022.3141437.

[2] B. Park et al., "The magnetic energy harvester with improved power density using saturable magnetizing inductance model for maintenance applications near high voltage power line," *IEEE Access*, vol. 9, pp. 82661–82674, 2021, doi: 10.1109/ACCESS.2021.3085989.

[3] O. B. Akan, O. Cetinkaya, C. Koca, and M. Ozger, "Internet of hybrid energy harvesting things," *IEEE Internet Things J.*, vol. 5, no. 2, pp. 736–746, Apr. 2018, doi: 10.1109/JIOT.2017.2742663.

[4] J. Chu et al., "Identification of gas mixtures via sensor array combining with neural networks," *Sensors Actuators B, Chem.*, vol. 329, 2021, Art. no. 129090, doi: 10.1016/j.snb.2020.129090.

[5] G. S. Dhunna and I. Al-Anbagi, "A low power WSNs attack detection and isolation mechanism for critical smart grid applications," *IEEE Sensors J.*, vol. 19, no. 13, pp. 5315–5324, Jul. 2019, doi: 10.1109/JSEN.2019.2902357.

[6] J. Chu et al., "Fault diagnosis of SF_6-insulated equipment by micro gas sensor array," *IEEE Trans. Power Del.*, vol. 38, no. 1, pp. 222–230, Feb. 2023, doi: 10.1109/TPWRD.2022.3184687.

[7] J. Chu et al., "Method of sieving the optimal NO_2 sensitive material," *Sensors Actuators B, Chem.*, vol. 375, 2023, Art. no. 132929, doi: 10.1016/j.snb.2022.132929.

[8] C. Jiang et al., "Wireless technologies for energy harvesting and transmission for ambient self-powered systems," *ACS Nano*, vol. 15, no. 6, pp. 9328–9354, 2021, doi: 10.1021/acsnano.1c02819.

[9] F. K. Shaikh and S. Zeadally, "Energy harvesting in wireless sensor networks: A comprehensive review," *Renewable Sustain. Energy Rev.*, vol. 55, pp. 1041–1054, 2016, doi: 10.1021/acsnano.1c02819.

[10] X. Zhao et al., "A soft magnetoelastic generator for wind-energy harvesting," *Adv. Mater.*, vol. 34, no. 38, 2022, Art. no. 2204238, doi: 10.1002/adma.202204238.

[11] C. R. Chowdhury, C. Mandal, and S. Misra, "Sustainable maintenance of connected dominating set by solar energy harvesting for IoT networks," *IEEE Trans. Green Commun. Netw.*, vol. 6, no. 4, pp. 2115–2127, Dec. 2022, doi: 10.1109/TGCN.2022.3175035.

[12] O. López-Lapeña, "Time-division multiplexing control of multi-input converters for low-power solar energy harvesters," *IEEE Trans. Ind. Electron.*, vol. 65, no. 12, pp. 9668–9676, Dec. 2018, doi: 10.1109/TIE.2018.2821622.

[13] A. Rahman, O. Farrok, M. R. Islam, and W. Xu, "Recent progress in electrical generators for oceanic wave energy conversion," *IEEE Access*, vol. 8, pp. 138595–138615, 2020, doi: 10.1109/ACCESS.2020.3012662.

[14] C. Wei and X. Jing, "A comprehensive review on vibration energy harvesting: Modelling and realization," *Renewable Sustain. Energy Rev.*, vol. 74, pp. 1–18, 2017, doi: 10.1016/j.rser.2017.01.073.

[15] T. Yang et al., "Nonlinear vibration energy harvesting and vibration suppression technologies: Designs, analysis, and applications," *Appl. Phys. Rev.*, vol. 8, no. 3, 2021, Art. no. 031317, doi: 10.1063/5.0051432.

[16] H. Jouhara et al., "Thermoelectric generator (TEG) technologies and applications," *Int. J. Thermofluids*, vol. 9, 2021, Art. no. 100063, doi: 10.1016/j.ijft.2021.100063.

[17] O. Cetinkaya and O. B. Akan, "Electric-field energy harvesting in wireless networks," *IEEE Wireless Commun.*, vol. 24, no. 2, pp. 34–41, Apr. 2017, doi: 10.1109/MWC.2017.1600215.

[18] S. Yuan, Y. Huang, J. Zhou, Q. Xu, C. Song, and G. Yuan, "A high-efficiency helical core for magnetic field energy harvesting," *IEEE Trans. Power Electron.*, vol. 32, no. 7, pp. 5365–5376, Jul. 2017, doi: 10.1109/TPEL.2016.2610323.

[19] X. Zeng, Z. Yang, P. Wu, L. Cao, and Y. Luo, "Power source based on electric field energy harvesting for monitoring devices of high-voltage transmission line," *IEEE Trans. Ind. Electron.*, vol. 68, no. 8, pp. 7083–7092, Aug. 2021, doi: 10.1109/TIE.2020.3003551.

[20] Z. Liu, Y. Li, H. Yang, N. Duan, and Z. He, "An accurate model of magnetic energy harvester in the saturated region for harvesting maximum power: Analysis, design, and experimental verification," *IEEE Trans. Ind. Electron.*, vol. 70, no. 1, pp. 276–285, Jan. 2023, doi: 10.1109/TIE.2022.3156033.

[21] D. Monagle, E. Ponce, and S. B. Leeb, "Generalized analysis method for magnetic energy harvesters," *IEEE Trans. Power Electron.*, vol. 37, no. 12, pp. 15764–15773, Dec. 2022, doi: 10.1109/TPEL.2022.3195149.

[22] J. Moon and S. B. Leeb, "Analysis model for magnetic energy harvesters," *IEEE Trans. Power Electron.*, vol. 30, no. 8, pp. 4302–4311, Aug. 2015, doi: 10.1109/TPEL.2014.2357448.

[23] Y. Ding, Y. C. Tian, X. Li, Y. Mishra, G. Ledwich, and C. Zhou, "Constrained broadcast with minimized latency in neighborhood area networks of smart grid," *IEEE Trans. Ind. Inform.*, vol. 16, no. 1, pp. 309–318, Jan. 2020, doi: 10.1109/TII.2019.2915826.

[24] Y. Zhuang et al., "Improving current transformer-based energy extraction from AC power lines by manipulating magnetic field," *IEEE Trans. Ind. Electron.*, vol. 67, no. 11, pp. 9471–9479, Nov. 2020, doi: 10.1109/TIE.2019.2952795.

[25] Z. Liu et al., "A novel method for magnetic energy harvesting based on capacitive energy storage and core saturation modulation," *IEEE Trans. Ind. Electron.*, vol. 70, no. 3, pp. 2586–2595, Mar. 2023, doi: 10.1109/TIE.2022.3172777.

[26] J. Moon and S. B. Leeb, "Power electronic circuits for magnetic energy harvesters," *IEEE Trans. Power Electron.*, vol. 31, no. 1, pp. 270–279, Jan. 2016, doi: 10.1109/TPEL.2015.2401336.

[27] J. Moon and S. B. Leeb, "Power loss analysis with high primary current in magnetic energy harvesters," in *Proc. IEEE 16th Workshop Control Model. Power Electron.*, 2015, pp. 1–8, doi: 10.1109/COMPEL.2015.7236503.

[28] Y. Zhuang et al., "An improved energy harvesting system on power transmission lines," in *Proc. IEEE Wireless Power Transf. Conf.*, 2017, pp. 1–3, doi: 10.1109/WPT.2017.7953847.

[29] S. Paul, S. Bashir, and J. Chang, "Design of a novel electromagnetic energy harvester with dual core for deicing device of transmission lines," *IEEE Trans. Magn.*, vol. 55, no. 2, Feb. 2019, Art. no. 8000104, doi: 10.1109/TMAG.2018.2873012.

[30] W. Wang, C. Xu, C. Zhang, and C. Chen, "Start-up and saturation optimization of high-power energy harvester with compound topologies overhead AC transmission line," *IEEE J. Emerg. Sel. Topics Power Electron.*, vol. 8, no. 4, pp. 3609–3617, Dec. 2020, doi: 10.1109/JESTPE.2019.2941970.
[31] A. A. Gaikwad and S. B. Kulkarni, "Evaluation of dimensional effect on electromagnetic energy harvesting," *Procedia Comput. Sci.*, vol. 143, pp. 58–65, 2018, doi: 10.1016/j.procs.2018.10.351.
[32] Y. Li, N. Duan, Z. Liu, J. Hu, and Z. He, "Impedance-matching-based maximum power tracking for magnetic field energy harvesters using active rectifiers," *IEEE Trans. Ind. Electron.*, vol. 70, no. 10, pp. 10730–10739, Oct. 2023, doi: 10.1109/TIE.2022.3219064.
[33] T.-C. Huang et al., "120% Harvesting energy improvement by maximum power extracting control for high sustainability magnetic power monitoring and harvesting system," *IEEE Trans. Power Electron.*, vol. 30, no. 4, pp. 2262–2274, Apr. 2015, doi: 10.1109/TPEL.2014.2330868.
[34] M. Gao, L. Yi, and J. Moon, "Mathematical modeling and validation of saturating and clampable cascaded magnetics for magnetic energy harvesting," *IEEE Trans. Power Electron.*, vol. 38, no. 3, pp. 3455–3468, Mar. 2023, doi: 10.1109/TPEL.2022.3218725.
[35] L. Costanzo, A. L. Schiavo, and M. Vitelli, "Design guidelines for the perturb and observe technique for electromagnetic vibration energy harvesters feeding bridge rectifiers," *IEEE Trans. Ind. Appl.*, vol. 55, no. 5, pp. 5089–5098, Sep./Oct. 2019, doi: 10.1109/TIA.2019.2923162.
[36] A. Brenes et al., "Maximum power point of piezoelectric energy harvesters: A review of optimality condition for electrical tuning," *Smart Mater. Struct.*, vol. 29, no. 3, 2020, Art. no. 033001, doi: 10.1088/1361-665X/ab6484.
[37] M. Shim, J. Kim, J. Jeong, S. Park, and C. Kim, "Self-powered 30 μw to 10 mW piezoelectric energy harvesting system with 9.09 ms/V maximum power point tracking time," *IEEE J. Solid-State Circuits*, vol. 50, no. 10, pp. 2367–2379, Oct. 2015, doi: 10.1109/JSSC.2015.2456880.
[38] N. Kong and D. S. Ha, "Low-power design of a self-powered piezoelectric energy harvesting system with maximum power point tracking," *IEEE Trans. Power Electron.*, vol. 27, no. 5, pp. 2298–2308, May 2012, doi: 10.1109/TPEL.2011.2172960.
[39] L. Costanzo, A. L. Schiavo, and M. Vitelli, "A self-supplied power optimizer for piezoelectric energy harvesters operating under non-sinusoidal vibrations," *Energies*, vol. 16, no. 11, 2023, Art. no. 4368, doi.org/10.3390/en16114368

Kai Ye was born in China in 1999. He received the B.S. degree in electrical engineering in 2021 from Xi'an Jiaotong University, Xi'an, China, where he is currently working toward the M.S. degree in electrical engineering with the Department of Electrical Engineering.

His current research interests include current transformer–based energy harvesting and wireless power transfer technology.

Zhu Liu was born in China in 1999. He received the B.S. degree in electrical engineering in 2020 from Xi'an Jiaotong University, Xi'an, China, where he is currently working toward the Ph.D. degree in electrical engineering with the Department of Electrical Engineering.

His main research interests include magnetic energy harvesting and wireless power transfer.

Chujun Liu was born in Changchun, China, in 1997. She received the B.S. degree in electrical engineering from Jilin University, Changchun, China, in 2020. She is currently working toward the M.S. degree in electrical engineering with Xi'an Jiaotong University, Xi'an, China.

Her research interests include magnetic energy harvesting and wireless power transfer.

Aijun Yang (Senior Member, IEEE) received the B.S. and Ph.D. degrees in electrical engineering from Xi'an Jiaotong University, Xi'an, China, in 2009 and 2014, respectively.

He is currently a Professor with Xi'an Jiaotong University. His main research interests include condition monitoring techniques, energy harvesters, and fault diagnosis.

Huan Yuan received the B.S. degree in electrical engineering from Southwest Jiaotong University, Chengdu, China, in 2014, and the Ph.D. degree in electrical engineering from Xi'an Jiaotong University, Xi'an, China, in 2019.

He is currently an Assistant Professor with Xi'an Jiaotong University. His main research interests include energy harvesting, wireless power transfer, fault diagnosis, and artificial intelligence.

Mingzhe Rong (Senior Member, IEEE) received the B.S. and Ph.D. degrees in electrical engineering from Xi'an Jiaotong University, Xi'an, China, in 1984 and 1990, respectively.

He is currently a Professor with Xi'an Jiaotong University. His main research interests include the detection and diagnosis techniques for electrical equipment and online monitoring techniques.

Dr. Rong is an IET Fellow.

Xiaohua Wang (Senior Member, IEEE) received the B.S. degree in electrical engineering from Chang'an University, Xi'an, China, in 2000, and the Ph.D. degree in electrical engineering from Xi'an Jiaotong University, Xi'an, China, in 2006.

He is currently a Professor with Xi'an Jiaotong University. His main research interests include condition monitoring techniques, fault diagnosis, and energy harvesters.